Chinese Chemical Letters 33 (2022) 5200–5207

Contents lists available at ScienceDirect

Chinese Chemical Letters

journal homepage: www.elsevier.com/locate/cclet

Novel organic/inorganic PDI-Urea/BiOBr S-scheme heterojunction for improved photocatalytic antibiotic degradation and H_2O_2 production

Weiwei Wang[a], Xibao Li[a,b,*], Fang Deng[b], Jiyou Liu[a], Xiaoming Gao[c], Juntong Huang[a], Jilin Xu[a], Zhijun Feng[a], Zhi Chen[a], Lu Han[d,*]

[a] School of Materials Science and Engineering, Nanchang Hangkong University, Nanchang 330063, China
[b] Key Laboratory of Jiangxi Province for Persistent Pollutants Control and Resources Recycle, Nanchang Hangkong University, Nanchang 330063, China
[c] Department of Chemistry and Chemical Engineering, Shaanxi Key Laboratory of Chemical Reaction Engineering, Yan'an University, Yan'an 716000, China
[d] School of Materials and Metallurgy, University of Science and Technology Liaoning, Anshan 114051, China

ARTICLE INFO

Article history:
Received 20 October 2021
Revised 10 December 2021
Accepted 23 January 2022
Available online 31 January 2022

Keywords:
Photocatalysis
Perylene diimide
Bismuth bromide oxide
S-scheme heterojunction
Antibiotic

ABSTRACT

The matched energy band structure and efficient carrier separation efficiency are the keys to heterogeneous photocatalytic reactions. A novel organic/inorganic step scheme (S-scheme) heterojunction PDI-Urea/BiOBr composite photocatalyst was constructed by simple solvothermal reaction combined with *in-situ* growth strategy. The composite photocatalyst not only has high chemical stability, but also can generate and accumulate a large number of active species (h^+, $^{\cdot}O_2^-$, $^{\cdot}OH$, H_2O_2). PDI-Urea/BiOBr showed higher photocatalytic activity for the degradation of antibiotic such as ofloxacin (OFLO), tetracycline (TC) and the production of H_2O_2 in the spectral range of 400–800 nm. The apparent rate constant of 15% PDI-Urea/BiOBr for photocatalytic degradation of TC (or OFLO) was 2.7 (or 2.5) times that of pure BiOBr and 1.7 (or 1.8) times that of pure PDI-Urea. The H_2O_2 evolution rate of 15% PDI-Urea/BiOBr was 2.5 times that of PDI-Urea and 1.5 times that of BiOBr, respectively. This work has formed a mature S-scheme heterojunction design thought and method, which offers new visions for the development of heterogeneous photocatalysts.

Environmental governance and the development of efficient and sustainable renewable energy are two major problems in the current social development [1–4]. In recent years, the research on antibiotic pollution in the environment has gradually increased, however, the conversion and removal of common antibiotics such as tetracycline (TC) [5–8], ciprofloxacin [9–11], ofloxacin (OFLO) [12–14], oxytetracycline [15,16], erythromycin [17] and penicillin [18] is still a thorny problem. These antibiotics are directly discharged into natural water after being used as drugs [19–23]. Since these drugs are not biodegradable, some of the residual antibiotics can accumulate in water and eventually endanger the whole ecosystem including human beings [24–27]. It is urgent to degrade antibiotic pollutants. In addition, with the increasingly stringent carbon emission standards, looking for new efficient and clean technologies to produce energy will also become our research hotspot [28–31]. Photocatalytic technology has many advantages, such as low cost, no secondary pollution, high efficiency, high reuse rate [32–37]. It is the best candidate to solve the above two problems. However, the research of photocatalytic materials still faces many problems, such as low utilization rate of solar energy and ineffective separation of photogenerated carriers [38–43]. High-efficiency and high-stability photocatalytic materials are expected to be studied.

Perylene diimide (PDI) is an organic semiconductor with abundant resources, easily controlled morphology, diverse chemical structure and function [44–46]. It has been proved that the energy band structure and internal electric field (IEF) of photocatalyst can be adjusted by the frontier orbital energy level and dipole of the molecule [47–50]. PDI molecule is assembled into supramolecule by linking with urea, which has strong stability and high photocatalytic performance [51]. PDI supramolecular has been paid more and more attention due to its small band gap and wide spectral response [52,53]. Zhang *et al.* [54] synthesized PDI-Urea showed a very high oxygen production rate (3223.9 μmol g^{-1} h^{-1}) under visible light irradiation, which is 107.5 times higher than that of the previous PDI supramolecular photocatalysts. PDI-Urea was pretty stable in this process, and the photocatalytic activity almost did not decrease after 100 h of continuous irradiation. The covalent

* Corresponding authors.
E-mail addresses: lixibao@nchu.edu.cn (X. Li), hanlu@ustl.edu.cn (L. Han).

https://doi.org/10.1016/j.cclet.2022.01.058
1001-8417/

bond assembly greatly promotes the directional transfer of charge in PDI-Urea supramolecular.

BiOBr is the most deeply studied inorganic photocatalyst in bismuth oxyhalide semiconductors. Despite some shortcomings, such as wide band gap, and narrow visible light response range [55], the IEF formed by the dipole in the BiOBr molecule promotes the effective separation of photogenerated electron-hole pairs, therefore, BiOBr has excellent photocatalytic activity [56–58]. Yao *et al.* [59] synthesized black phosphorus quantum dots/bismuth oxybromide (BPQDs/BiOBr) Z-scheme heterojunction by hydrothermal method combined with surface modification strategy to improve the degradation performance of BiOBr films. The photocatalytic activity of BPQDs/BiOBr-1 film with the best ratio for TC degradation is 4.65 times that of pure BiOBr film. Juntrapirom *et al.* [60] prepared a TiO_2/BiOBr photocatalyst with natural light response. Under normal temperature and pressure, the green organic synthesis was carried out by using solar energy. *N,N'*-Dimethylbenzylamine was prepared by oxidation of coupling benzylamine, and the yield of imine within 1 h was about 89.0%. Its excellent photocatalytic activity is mainly attributed to the construction of II-scheme heterojunction, which expands the light response range and promotes effective charge separation and transfer.

The construction of heterojunctions such as Z-scheme and II-scheme can accelerate the separation and transfer of photogenerated carriers, while the S-scheme heterojunction photocatalyst realizes the spatial separation of semiconductor photogenerated electron holes under strong redox ability and high photocatalytic activity [61–63]. Liu *et al.* [64] has prepared 2D/2D WO_3/BiOBr S-scheme heterojunction by hydrothermal method. WO_3/BiOBr can remove 98% of TC in 60 min with PMS assisting under visible light. Ji *et al.* [65] has constructed a band gap matched n-n semiconductor BiOCl/PDI heterojunction, which has greatly improved the photodegradation performance of phenol, methyl orange, rhodamine B and other pollutants. This work fully demonstrates that the combination of π-conjugated organic and traditional inorganic semiconductors is a promising strategy for the design of novel S-scheme heterojunction photocatalysts.

The introduction of PDI-Urea into the BiOBr precursor solution enables the *in-situ* growth of BiOBr on PDI-Urea utilizing the characteristic high temperature and high pressure closed environment of solvothermal reaction. During this process, PDI-Urea could be firmly anchored on the BiOBr nanocrystals, thus forming a close interfacial contact between the two components. Such interfacial interactions are stronger than those between inorganic semiconductors dominated only by weak van der Waals forces, thus facilitating interfacial charge transfer. In this work, PDI-Urea/BiOBr S-scheme heterojunction with close interface was constructed by solvothermal *in-situ* growth strategy. The construction strategy of heterojunction promotes the transfer of photogenerated electrons and enhances the light harvesting ability of the whole photocatalyst. Then, the study focused on the photocatalytic activity of the as-prepared photocatalysts for the degradation of TC, OFLO and the production of H_2O_2. In addition, the photocatalytic mechanism and quantitative structure activity relationship (QSAR) of PDI-Urea/BiOBr S-scheme heterojunction composite photocatalyst was discussed.

PDI-Urea was prepared by a facile heated reflux method. 0.120 g of urea (2.0 mmol), 0.780 g of perylene-3,4,9,10-tetracarboxylic dianhydride (PA, 2.0 mmol), 0.370 g of anhydrous zinc acetate (2.0 mmol) and 5.0 g of imidazole were mixed and carefully put into a 100.0 mL three port flask. Under the protection of argon, the mixed solution was heated at 150 °C for about 5 h and stirred at a constant speed. When the temperature dropped to room temperature, 250.0 mL HCl solution (1.0 mol/L) was added. Then the mixed solution was stirred overnight. After the HCl solution was removed, it was washed with DI water until it was neutral, and then washed with dimethyl sulfoxide (DMSO) for about three times until the washing liquid became colorless. After vacuum drying, a crimson and highly insoluble product was obtained, marked as PDI-Urea. The synthesis reaction strategy is shown in Fig. S1 (Supporting information).

Light yellow BiOBr powder was synthesized by solvothermal method. At first, 0.485 g of $Bi(NO_3)_3{\cdot}5H_2O$ (1.0 mmol) was added to 50.0 mL of ethylene glycol. The stirred solution was heated to about 40 °C until $Bi(NO_3)_3{\cdot}5H_2O$ was completely dissolved. The liquid obtained was designated as solution A. Then 0.119 g KBr (1.0 mmol) was added into 20.0 mL ethylene glycol. The obtained solution was recorded as solution B. The solution B was slowly dropped into solution A and the mixed solution was stirred for 0.5 h. The precursor solution was fed into the lining of 100.0 mL reactor and subjected to solvent heat treatment at 200 °C for 24 h. After cooling, the precipitate is separated, collected and dried in vacuum. The resulting straw yellow powder was labeled as BiOBr.

The preparation process of PDI-Urea/BiOBr composite photocatalyst was basically the same as that of BiOBr. After mixing solution A and B and keeping stirring, a certain amount of as-prepared PDI-Urea dark red powder (0.016 g, 0.054 g, 0.102 g and 0.164 g, respectively) was added. The final powder was labeled as X%PDI-Urea/BiOBr (X% represents the mass percentage of PDI-Urea molecule in the composite photocatalyst, which are 5%, 15%, 25% and 35%, respectively).

The phase composition of photocatalysts was characterized by Bruker D8 Advance X-ray diffraction (XRD) with Cu Kα (λ = 0.1541 nm) radiation. The Fourier transform infrared spectroscopy (FT-IR) spectra were investigated with a Bruker VERTEX 70 spectrometer. The microstructures and mapping were observed by the FEI Nova Nano SEM450 scanning electron microscope (SEM) and the FEI Talos F200X transmission electron microscopy (TEM) with energy dispersive X-ray spectrometer (EDS). The infrared spectra including the structural composition and chemical functional groups of the samples were obtained by Nicolet NEXUS 670 spectrometer (Thermo Co., Ltd., Madison, WI, USA). The chemical states were analyzed by the Shimadzu Axis Ultra DLD X-ray photoelectron spectroscopy (XPS) with Al Kα radiation. The ultraviolet visible diffuse reflectance spectroscopy (UV–vis-DRS) was detected by the Shanghai Metash UV-9000 ultraviolet visible spectrophotometer equipped with an integrating sphere. Electrochemical analyzer with three-electrode system (Chenhua CHI760E, Shanghai, China) was employed to analyze the photoelectrochemical properties. In addition, Ag/AgCl electrode, Pt sheet (20 × 20 × 0.1 mm^3), and carbon paper coated with photocatalyst (1 × 1.5 cm^2, HCP030 N, Shanghai Hesen, China) were used as the reference electrode, counter electrode and working electrode, respectively. A 300 W xenon lamp (PerfectLight PLS-SXE300/300UV, Beijing, China) was used as visible light source and 0.5 mol/L Na_2SO_4 solution as electrolyte. Electrochemical impedance spectroscopy (EIS), Mott Schottky curve (MS) and photocurrent response curve were measured on an electrochemical analyzer. Electron spin resonance (ESR) spectra were recorded on a JEOL FA-200 spectrometer. The Brunauer-Emmett-Teller (BET) surface areas and pore distributions were measured using a 3H-2000PM2 isothermal N_2 adsorption analyzer (Beishide, Beijing, China). The fluorescence excitation emission spectra of the samples were measured by a FLS1000 fluorescence spectrophotometer (Edinburgh, British). The time-resolved fluorescence decay spectra were recorded on the Hitachi F-7100 fluorescence spectrometer.

Density functional theoretical calculation. The work function (Φ) was calculated by density functional theory (DFT). The calculations of electronic properties and geometric optimization were realized in Dmol code of Materials Studio (MS) software using DFT. The exchange correlation of electrons was performed by the gener-

alized gradient approximation (GGA) method with Perdew-Burke-Ernzerhof (PBE). For the construction of surface models, a vacuum of 15 Å was used to eliminate interactions between periodic images. The Φ calculations were carried out using Vienna ab initio simulation package (VASP).

A 300 W xenon lamp was used to simulate the sunlight, and the range of visible light was 420 nm to 780 nm. The target pollutants of photocatalysis were TC (50 mg/L) and OFLO (10 mg/L). Specifically, 50 mg photocatalyst is placed in a quartz bottle before adding 50 mL target pollutant solution. The concentration of the reaction product was determined by high performance liquid chromatography (Shimadzu LC-20A). The concentration of H_2O_2 produced by photocatalysis was determined by iodine titration [22,25].

The crystal structures and phases of BiOBr, PDI-Urea and 15% PDI-Urea/BiOBr were studied by XRD. As shown in Fig. S2a (Supporting information), the strong response diffraction peaks of BiOBr, PDI-Urea and 15% PDI-Urea/BiOBr samples were observed, indicating that the prepared samples were highly crystalline. The diffraction peaks of the XRD patterns of the prepared samples can correspond to (001), (012), (110) and (003) of BiOBr (JCPDS card No. 09–0393) and Bi metal (JCPDS card No. 05–0519), and no other redundant diffraction peaks were detected, which indicates that the purity of BiOBr prepared by glycol solvothermal method is very high. Significantly, the strong diffraction peaks (2θ = 27.2°) can be attributed to Bi metal, caused by the reason that part of Bi^{3+} is reduced to Bi metal by glycol at 200 °C [66]. The XRD diffraction peak corresponding to 27.2° of PDI-Urea can be attributed to the π-π interaction, indicating that there is a stacking structure in PDI-Urea [54]. The face-to-face overlapped delocalized electron cloud formed by the π-π interaction can be used as an electron channel to accelerate the electron transfer between molecules. For 15% PDI-Urea/BiOBr, almost all diffraction peaks of BiOBr are retained. However, the XRD diffraction peak intensity of PDI-Urea has decreases obviously, which can be explained by the fact that the content of PDI-Urea in 15% PDI-Urea/BiOBr is relatively small, and BiOBr envelops or obscures PDI-Urea because it *in-situ* grows on the surface of PDI-Urea. Fig. S2b (Supporting information) shows an enlarged view of 25°–29° The relative shift of the XRD diffraction peaks of BiOBr, PDI-Urea and 15% PDI-Urea/BiOBr indicates that there is a certain interaction between PDI-Urea and BiOBr in 15% PDI-Urea/BiOBr synthesized by solvothermal method [67]. The XRD analysis shows that the PDI-Urea/BiOBr composite photocatalyst was obtained by solvothermal reaction.

All the samples were characterized by infrared spectroscopy (Fig. S2c in Supporting information). The characteristic peak of perylene anhydride monomer at 1770 cm^{-1} is attributed to the symmetrical tensile vibration of C=O bond in carbonyl group. PDI-Urea synthesized by self-assembly has no characteristic peak of perylene anhydride at 1770 cm^{-1}, and the peak position moves to 1686 cm^{-1} (contribution of N–C=O bond) to form a new strong response peak. This can be explained that due to the electronegativity of the bonding group and the conjugation effect of the polymer, the carbon group in the polymer experiences a significant change in bond strength [54]. In addition, the new peak at 1750 cm^{-1} in PDI-Urea is attributed to the carbonyl group connected with urea, and several new characteristic peaks (such as 663 cm^{-1}) appear, which indicates that PDI-Urea supramolecule is successfully synthesized from perylene anhydride. In the infrared spectra of the prepared composite, the intensity of the characteristic peaks at 1686 cm^{-1} and 1590 cm^{-1} gradually increases with the increase of PDI-Urea content, indicating that the distribution of PDI-Urea in PDI-Urea/BiOBr composite is relatively uniform. The peak of BiOBr at 520 cm^{-1} is due to the stretching vibration of Bi–O bond, and the peak at 1625 cm^{-1} is the contribution of the bending and stretching vibration of O–H bond caused by surface adsorbed water [68]. It is worth noting that the characteristic response peak of Bi–O bond at 520 cm^{-1} of BiOBr also appears in PDI-Urea/BiOBr, and the peak increases with the increase of BiOBr content, which indicates that PDI-Urea had no effect on the formation of BiOBr. The results of infrared spectrum analysis also show that the basic chemical structure of PDI-Urea was not destroyed under high temperature and high pressure at 200 °C, and PDI-Urea was successfully combined with BiOBr.

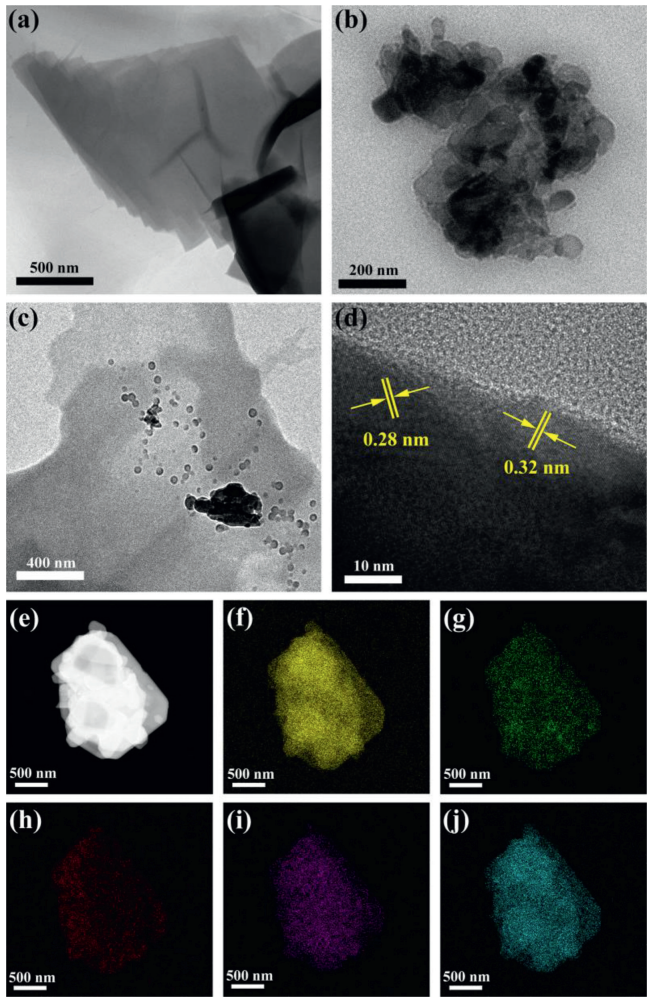

Fig. 1. TEM images of (a) PDI-Urea, (b) BiOBr and (c) PDI-Urea/BiOBr; (d) lattice fringe pattern of PDI-Urea/BiOBr complex; (e) micro constituency of PDI-Urea/BiOBr; elemental mapping of (f) C, (g) N, (h) O, (i) Br and (j) Bi.

The microscopic morphological analysis of PDI-Urea, BiOBr and PDI-Urea was carried out using SEM (Fig. S3 in Supporting information) and TEM (Fig. 1). As shown in Figs. 1a-c, PDI-Urea exhibits a stacked lamellar structure and BiOBr shows a nanosphere structure, and in the PDI-Urea/BiOBr complex, BiOBr nanospheres are dispersed on the PDI-Urea lamellar layer. A lattice stripe with a lattice spacing of 0.28 nm can be detected corresponding to the (102) crystal plane of BiOBr (Fig. 1d). The π-π stacking interaction between the PDI-Urea molecules can be confirmed by a lattice spacing of 0.32 nm, which corresponds to the diffraction peak of 27.2° in Fig. S2a. The element mapping in the PDI-Urea/BiOBr complex was analyzed (Fig. 1e) and the mappings of elemental distribution (Figs. 1f-j) were obtained for C, N, O, Br and Bi, which are uniformly dispersed in PDI-Urea/BiOBr.

The photocatalytic activity of the above samples was evaluated by photocatalytic degradation of antibiotics (TC, OFLO) and photocatalytic production of H_2O_2. Before each experiment, the sam-

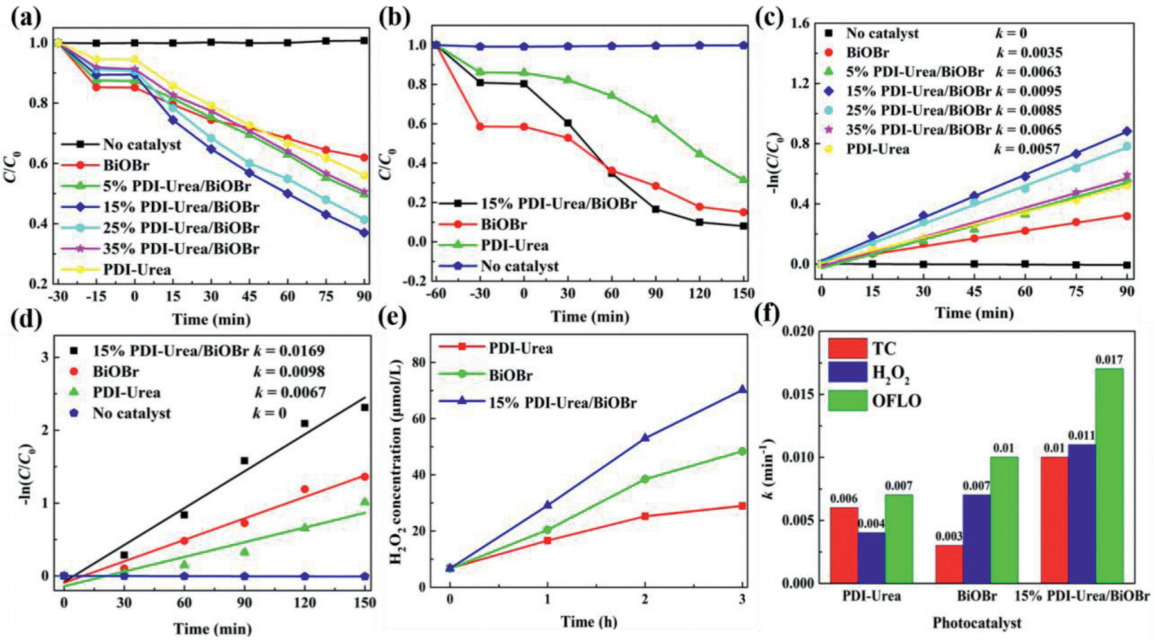

Fig. 2. (a) Photodegradation curves of TC under visible-light irradiation; (b) photodegradation curves of OFLO under visible-light irradiation; (c) the kinetics fitting curves of TC degradation by BiOBr, PDI-Urea and complexes with different ratios; (d) the kinetics fitting curves of OFLO degradation by BiOBr, PDI-Urea and 15% PDI-Urea/BiOBr; (e) concentration-time plots of BiOBr, PDI-Urea and 15% PDI-Urea/BiOBr for the photocatalytic production of H_2O_2; (f) summary of apparent rate constants of the photocatalytic degradation of TC, OFLO and the production of H_2O_2.

ples need to be dark treated for a certain time (marked as negative sign) to achieve dynamic adsorption-desorption equilibrium. The negligible degradation of TC and OFLO by the blank group without the addition of photocatalyst was observed in Figs. 2a and b, indicating that both TC and OFLO have high photostability and are perfectly feasible as target pollutants. Furthermore, it is observed from Fig. 2a that the photodegradation activity of the PDI-Urea/BiOBr composite photocatalyst for TC is significantly higher relative to either pure PDI-Urea or pure BiOBr. Among them, 15% PDI-Urea/BiOBr showed the best degradation rate of TC within 90 min. The primary reaction kinetic fitting curve (Fig. 2c) was obtained by transforming the data into a linear fit, where k is the slope of the fitted curve, which represents the apparent rate constant of the photocatalytic degradation. After 90 min of light illumination, the k value of photodegradation for TC by the 15% PDI-Urea/BiOBr sample was 2.7 times that of pure BiOBr and 1.7 times that of pure PDI-Urea, indicating a significant increase in the experimental photocatalytic reaction rate of the composite sample. In addition, the effects of TC degradation under different conditions, including catalyst dosage, TC solution concentration, and pH of the reaction solution on the photocatalytic performance were systematically investigated (Fig. S4 in Supporting information). When the dosage of 15% PDI-Urea/BiOBr sample increased from 0.8 g/L to 1.0 g/L, the degradation efficiency of TC was significantly improved. However, when the dosage of catalyst further increased, the degradation rate of TC began to decrease gradually. With the increase of TC concentration, the degradation rate decreased gradually, while at high TC concentration, the degradation rate decreased significantly. Furthermore, PDI is an organic semiconductor material modified by terminal carboxylic acid functional groups, which will lead to catalyst dissociation at high pH value. Under acidic conditions, the degradation rate of TC decreased with the decrease of pH value.

To verify the non-selective degradation for TC by the PDI-Urea/BiOBr composite photocatalyst, photocatalytic experiments of the degradation for OFLO were also carried out for PDI-Urea, BiOBr and 15% PDI-Urea/BiOBr. As shown in Fig. 2b, after light irradiation for 150 min, the 15% PDI-Urea/BiOBr photocatalyst achieved 93% photocatalytic degradation rate for OFLO compared to the control group with only PDI-Urea or BiOBr photocatalyst added, and its photocatalytic activity had greatly improved, which indicates that the PDI-Urea/BiOBr composite photocatalysts have a relative general photocatalytic activity and that the construction of PDI-Urea/BiOBr heterojunctions plays a key role. Fig. 2d shows the fitted curves of the primary reaction kinetics for the photocatalyst degradation experiments for OFLO. The apparent rate constants of the reaction of the photodegradation for OFLO by the 15% PDI-Urea/BiOBr samples reached 0.0169 min^{-1}, which was 2.5 times that of pure PDI-Urea and 1.8 times that of pure BiOBr. Interestingly, the difference in catalytic activity between PDI-Urea and BiOBr in the photocatalytic degradation for OFLO and degradation for TC experiments may be due to the stronger adsorption of OFLO by BiOBr, which increases the chance of collision of the reactive radicals generated by the reaction with the pollutant. The moderate amount of adsorption performance may be an important factor in the enhanced performance of the photocatalyst. In order to prove the above experimental results, the N_2 adsorption-desorption analysis of BiOBr and complexes was carried out (Fig. S5 in Supporting information).

The concentrations of BiOBr, PDI-Urea, and 15% PDI-Urea/BiOBr photocatalytic *in-situ* production of H_2O_2 were examined using the iodometric method (Fig. 2e). 15% PDI-Urea/BiOBr exhibited the best photocatalytic activity for the production of H_2O_2. After visible light irradiation for 3 h, H_2O_2 concentration in the reactor reached 71 μmol/L, which was 2.5 times that of PDI-Urea and 1.5 times that of BiOBr, respectively. Moreover, the apparent rate constants of the 15% PDI-Urea/BiOBr composite photocatalyst with BiOBr and PDI-Urea in photocatalytic degradation and H_2O_2 production experiments can be more intuitively compared by histogram (Fig. 2f). The results indicate that 15% PDI-Urea/BiOBr obtained by solvothermal treatment has significant advantages in the above photocatalytic experiments, and the design of heterojunction improves the sep-

aration efficiency of photogenerated carriers and photocatalytic activity.

In order to verify whether the 15% PDI-Urea/BiOBr has good photostability with high cycle availability, a cycle stability test was carried out. Subsequently, the 15% PDI-Urea/BiOBr samples before and after the reaction were characterized analytically accordingly (Fig. S6 in Supporting information). As shown in Fig. S6a, the photocatalytic degradation efficiency of 15% PDI-Urea/BiOBr for TC could still reach 96.6% of the first time after three cycles, which indicates that the stability of the composite photocatalyst is pretty well, and the existence of slight differences may be due to the catalyst not being thoroughly washed and purified during the separation and recycling process, and the presence of a small amount of impurities. In addition, XRD (Fig. S6b), UV–vis DRS (Fig. S6c), FT-IR spectra (Fig. S6d) and TEM (Figs. S6e and f) of the 15% PDI-Urea/BiOBr photocatalyst recycled and treated before and after the stability test were examined. The results show that cycling the photocatalytic experiments many times has almost no effect on the crystal structure, light response range and chemical structure of the composite photocatalysts. In other words, 15% PDI-Urea/BiOBr prepared by solvothermal *in-situ* growth maintained a fairly stable photocatalytic performance, good structural stability and cycling stability during the photocatalytic degradation of TC.

BiOBr, PDI-Urea and 15% PDI-Urea/BiOBr powder samples were made into electrodes, and relevant electrochemical analysis was carried out under visible light irradiation to further discuss the effect of heterostructure on the photocatalytic activity of the 15% PDI-Urea/BiOBr composite photocatalyst in terms of charge transfer resistance. As shown in Fig. S7a (Supporting information), the average transient photocurrents of BiOBr and PDI-Urea under visible light irradiation was only 0.6 μA and 1.1 μA, respectively. The average transient photocurrents (2.1 μA) of 15% PDI-Urea/BiOBr significantly increased. Similar results can also be derived from the electrochemical impedance spectrogram (Fig. S7b in Supporting information). The radius of the arc represents the intrinsic resistance of the material. 15% PDI-Urea/BiOBr shows less resistance to charge transfer. The excellent photochemical performance of the 15% PDI-Urea/BiOBr heterojunction is due to the minimal resistance to photogenerated charge transfer between PDI-Urea and BiOBr.

As is well known, the fluorescence emission can be formed by the recombination of electron-hole pairs, so the lower intensity of PL indicates lower recombination of e^--h^+ pairs. Fig. S8a (Supporting information) shows the PL spectra of BiOBr, PDI-Urea and 15% PDI-Urea/BiOBr. There was an obvious fluorescence signal at 470 nm for pure BiOBr. However, the intensity of emission peak decreased after combination with PDI-Urea, implying that the heterojunction PDI-Urea/BiOBr could facilitate the separation of e^--h^+ pairs. In addition, the time-resolved fluorescence decay spectra was applied to gain more insight into the photogenerated charge efficiency of PDI-Urea/BiOBr composites (Fig. S8b in Supporting information). The results show that the lifetime of 15% PDI-Urea/BiOBr (15.73 ns) is higher than that of the main component BiOBr (14.34 ns). The longer fluorescence lifetime of the composite sample means that the exciton dissociation and diffusion distance are enhanced, so more effective electron-hole pairs can be separated.

In order to investigate the photocatalytic mechanism of PDI-Urea/BiOBr, the energy band structure of BiOBr and PDI-Urea need to be analysed as a priority. Therefore, the MS curves (Figs. S9a and b in Supporting information) of BiOBr and PDI-Urea were also examined and analysed during the photochemical experiments. The MS curves at 0.5, 1.0 and 1.5 kHz were examined and the straight line sections were extended to the horizontal axis, obtained flat-band potentials (E_f) of BiOBr is 0.18 V (*vs.* Ag/AgCl, pH 7) and PDI-Urea is −0.13 V (*vs.* Ag/AgCl, pH 7), respectively. Based on $E_{NHE} = E_{Ag/AgCl} + 0.197$, the E_f of BiOBr and PDI-Urea were calculated to be approximately 0.38 V (*vs.* NHE, pH 7) and 0.07 V (*vs.* NHE, pH 7), respectively. In addition, the slope of the straight line portion of the MS curves for BiOBr and PDI-Urea is positive, indicating that both BiOBr and PDI-Urea have the characteristics of n-type semiconductors.

The photoresponse properties of the prepared samples were analysed by UV–vis DRS (Fig. S9c in Supporting information). With the introduction of PDI-Urea, the absorption edge of the PDI-Urea/BiOBr composite photocatalyst red-shifted to around 800 nm, covering all the UV–vis region with part of the near infrared light region, indicating that the combination of BiOBr and PDI-Urea improved the solar energy utilization of the composite photocatalyst, which in turn facilitated the excitation and leap of photogenerated electrons. The forbidden band width plots (Tauc, Fig. S9d in Supporting information) were also obtained for BiOBr and PDI-Urea. The straight line portion of the curve is taken to extend to a point where the band gap axis intersects, corresponding to a value of 2.63 eV and 1.82 eV for the forbidden band width of the BiOBr and PDI-Urea semiconductors, respectively. According to $E_g = E_{VB} - E_{CB}$, the valence band potential (E_{VB}) of BiOBr can be obtained as 3.01 eV and the E_{VB} of PDI-Urea as 1.89 eV. From the perspective of energy band structure, the interleaved energy bands of the n-type semiconductor BiOBr and PDI-Urea can build heterojunction, which provides internal driving force for photoelectron transfer.

In order to study the formation mechanism of IEF at the interface between PDI-Urea and BiOBr, DFT calculations were performed and the work functions of PDI-Urea and BiOBr single molecules were obtained [69]. The Fermi energy levels are determined self-consistently and the corresponding vacuum potential is calculated as the limiting vacuum of the average potential at a distance of about 4.5 nm in the direction perpendicular to the surface [70–72]. As shown in Fig. S10a (Supporting information), the work function (Φ) of PDI-Urea is calculated to be 5.77 eV. In the simulations, a work function of 7.12 eV was calculated for BiOBr when the electrostatic potential was chosen as the reference (Fig. S10b in Supporting information). As shown in Fig. S10c (Supporting information), after the contact between PDI-Urea and BiOBr, electrons will spontaneously diffuse from PDI with smaller work function to BiOBr with larger work function to establish a new equilibrium. After reaching equilibrium, an electron depletion layer and an electron accumulation layer are formed near the interface between PDI-Urea and BiOBr, making PDI-Urea positively charged and BiOBr negatively charged, forming an IEF from PDI-Urea to BiOBr. The establishment of this electric field will promote the transfer of photogenerated electrons from BiOBr to PDI-Urea. In addition, when the two semiconductors are in contact, the Fermi energy levels will be arranged at the same energy level E_{f3}, which will bend the energy band of PDI-Urea and BiOBr, and cause the electrons on CB in BiOBr to recombine with the holes on VB in PDI-Urea. Moreover, due to the electrostatic interaction near the surface of the two components, different e^- and h^+ tend to recombine. In conclusion, the low energy electrons and holes were eliminated through the construction of S-scheme, while the powerful e^- and h^+ in CB of PDI-Urea and VB of BiOBr were retained to participate in the photocatalytic reaction.

The elemental species and valence states of 15% PDI-Urea/BiOBr were analysed by *in-situ* XPS and the binding energy change of 15% PDI-Urea/BiOBr was investigated to infer the electron transfer direction in the heterojunction [73–75]. As shown in Fig. 3a, the characteristic peaks associated with the elements C, N, O, Br and Bi can be found in the full spectrum, demonstrating the presence of BiOBr with PDI-Urea in 15% PDI-Urea/BiOBr. Fig. 3b shows the XPS spectrum of C 1s, the binding energy at 288.95 eV, 285.77 eV, 284.82 eV can be attributed to the C=O, N−C=O, C−C and C=C chemical bonding of the sp^2 or sp^3 hybridization of C

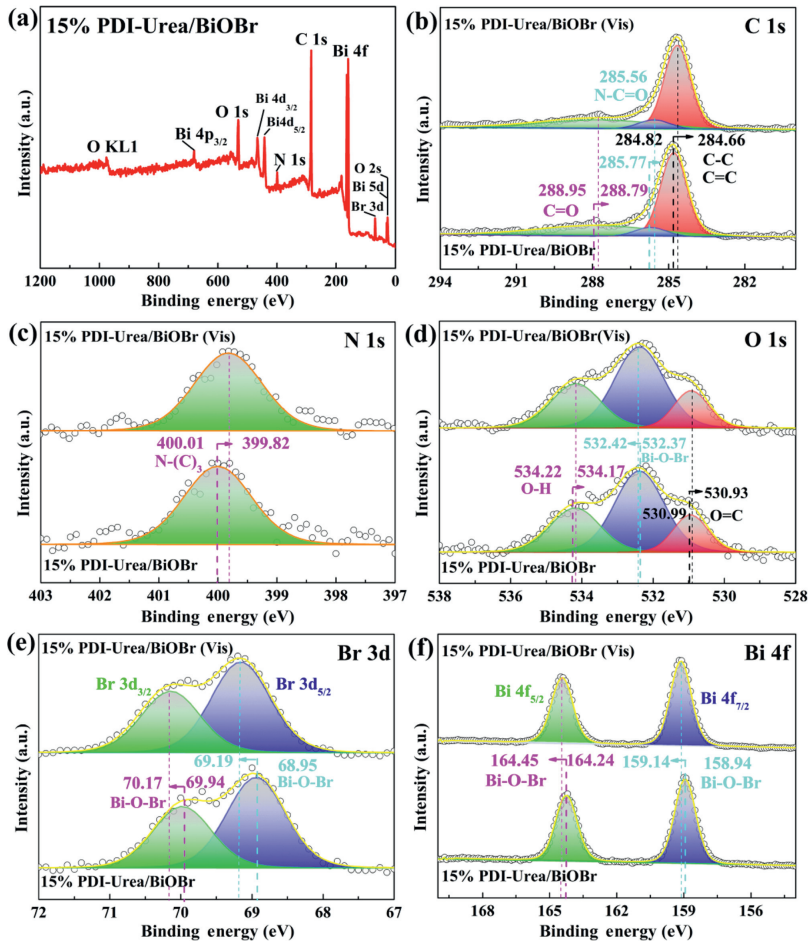

Fig. 3. (a) *In-situ* XPS spectra of full-spectrum; (b) C 1s, (c) N 1s, (d) O 1s, (e) Br 3d, (f) Bi 4f spectrum of 15% PDI-Urea/BiOBr.

in the 15% PDI-Urea/BiOBr heterojunction, respectively [54]. Fig. 3c shows the XPS spectrum of N 1s, with the only characteristic peak present at 400.01 eV attributed to the N–$(C)_3$ bond of the sp^2 hybridization. The XPS pattern of C 1s, N 1s reflects the chemical structure specific to the functional group of PDI-Urea in PDI-Urea/BiOBr. Fig. 3d shows the XPS spectrum of O 1s, the binding energies at 534.22 eV, 532.37 eV, 530.99 eV originate from the O–H bond in the binding water present on the surface of the 15% PDI-Urea/BiOBr heterojunction, the Bi–O–Br bond in BiOBr, the O=C functional group in PDI-Urea, respectively [76]. Fig. 3e shows the XPS spectrum of Br 3d The two characteristic peaks at binding energies of 69.94 eV and 68.95 eV are attributed to Br $3d_{3/2}$ and Br $3d_{5/2}$ in the Bi–O–Br bond, respectively [77]. Fig. 3f shows the XPS spectrum of Bi 4f. The characteristic peaks with binding energies of 164.24 eV, 158.94 eV correspond to Bi $4f_{5/2}$, Bi $4f_{7/2}$ in the Bi–O–Br bond [68]. Analysis of the XPS peaks of O 1s, Br 3d and Bi 4f reveals the elemental valence and chemical structure of the BiOBr substance.

Comparing the *in-situ* XPS of 15% PDI-Urea/BiOBr, it can be found that the peak positions of the XPS spectra of C 1s, N 1s, O 1s, Br 3d and Bi 4f have been significantly shifted, indicating that the electron density of each element in 15% PDI-Urea/BiOBr has changed. The position of the C=O functional group corresponding to the XPS peak under visible light irradiation is reduced from 288.95 eV to 288.79 eV. In addition, the position of the binding energy of the corresponding peak of N–$(C)_3$ is reduced from 400.01 eV to 399.82 eV. These results indicate that the electron density on the PDI-Urea of 15% PDI-Urea/BiOBr increases after light illumination. In the XPS pattern of Bi 4f, the peaks of Bi $4f_{5/2}$ and Bi $4f_{7/2}$ both shift to the left by about 0.20 eV. In the XPS pattern of Br 3d, the binding energies of the peaks corresponding to Br $3d_{3/2}$ and Br $3d_{5/2}$ increase by 0.23 eV and 0.24 eV, respectively, indicating a decrease in the electron density of BiOBr in the complex. This can be explained by the transfer of photogenerated electrons from BiOBr to PDI-Urea in 15% PDI-Urea/BiOBr under visible light irradiation. The results of the *in-situ* XPS analysis corroborate the conclusions of the DFT calculations and provide strong evidence for the direction of photogenerated electron transfer in the heterojunction.

AO, IPA and *p*-BQ were used as trapping agents for h^+, $^{\bullet}OH$ and $^{\bullet}O_2^-$, respectively. Radical capture experiments were carried out on 15% PDI-Urea/BiOBr photocatalysts for the degradation of TC to detect the main reactive radicals present during the photocatalytic reaction (Figs. 4a and b). After 90 min of light irradiation, 15% PDI-Urea/BiOBr photodegraded 58% of TC (after dark treatment), and the experimental groups with AO, IPA and *p*-BQ added before light irradiation had 37%, 50% and 25% removal rate of TC, respectively. The photocatalytic performance exhibited by the experimental groups was clearly inhibited. The photocatalytic degradation performance of 15% PDI-Urea/BiOBr decreased when AO, IPA and *p*-BQ were added, indicating that the corresponding reactive intermediates h^+, $^{\bullet}OH$ and $^{\bullet}O_2^-$ were involved in the degradation reactions of the pollutant. Some results were further confirmed by the detection of high activity $^{\bullet}OH$ and $^{\bullet}O_2^-$ with ESR measurements (Figs. 4c and d).

Based on above results, a possible photocatalytic reaction mechanism of PDI-Urea/BiOBr S-scheme heterojunction is proposed (Scheme 1). The analysis of the MS plots and Tauc Plots shows that

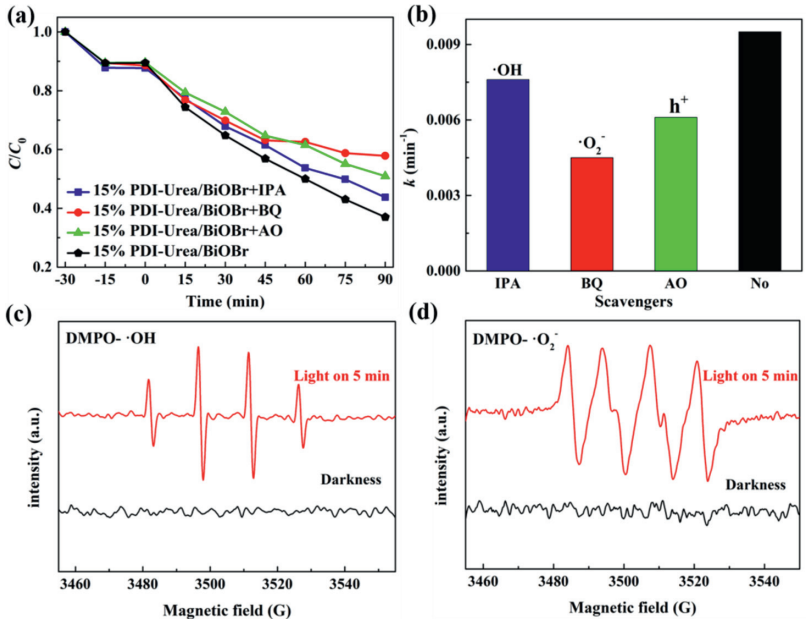

Fig. 4. (a) Free radical capture curves of 15% PDI-Urea/BiOBr and (b) the degradation rate constants *k* in radical scavenging experiments; (c, d) ESR spectra of $^{\bullet}OH$ and $^{\bullet}O_2^-$.

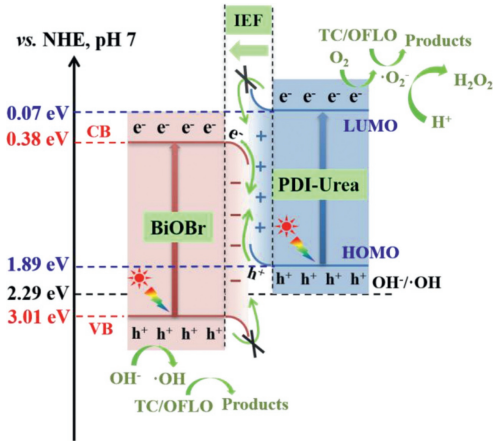

Scheme 1. S-scheme heterojunction photocatalytic mechanism of PDI-Urea/BiOBr photocatalyst.

the band gap structures of two n-type semiconductors, BiOBr and PDI-Urea, are interleaved and satisfy the basic conditions for the construction of S-scheme heterojunctions. Due to the difference of Fermi levels between BiOBr and PDI-Urea, electron transfer occurs in the heterojunction formed after the contact between them, and the energy band bending phenomenon occurs at the interface between them due to the accumulation and consumption of electrons, which facilitates the separation and transfer of electrons in the S-scheme PDI-Urea/BiOBr heterojunction. Based on the *in-situ* XPS results, it is known that the photogenerated electrons in the complex flow from BiOBr to PDI-Urea. In addition, the free radical capture experiments and ESR characterization show that $^{\bullet}OH$ radicals are present, indicating that the holes in the valence band of BiOBr are retained. Since the photoelectrons in the conduction band of BiOBr combine with the holes in the valence band of PDI-Urea, the photogenerated holes with strong oxidation on BiOBr and the photogenerated electrons with strong reduction on PDI-Urea are preserved, and they can be transferred to the surface to participate in the redox reaction of free radicals. The instant presence of strongly oxidizing $^{\bullet}OH$, h^+ and $^{\bullet}O_2^-$ at the reactive site on the surface of PDI-Urea/BiOBr rapidly oxidized and decomposed the antibiotics TC and OFLO. Furthermore, the conversion process from O_2 to H_2O_2 undergoes a sequential two-step single-electron processes ($O_2 + e^- \rightarrow {}^{\bullet}O_2^-$ and $^{\bullet}O_2^- + 2H^+ + e^- \rightarrow H_2O_2$) [78,79], the dissolved oxygen in the solution is reduced to strongly oxidized $^{\bullet}O_2^-$. Subsequently, H^+ in the aqueous solution combines with $^{\bullet}O_2^-$ to form $^{\bullet}OOH$. This $^{\bullet}OOH$ is further reduced by another e^- and combined with another H^+, resulting in a large amount of H_2O_2 products *in situ*.

In summary, PDI-Urea/BiOBr S-scheme heterojunction photocatalysts were prepared by *in-situ* growth method, and their enhanced photocatalytic activities and possible mechanisms were investigated. The organic/inorganic PDI-Urea/BiOBr S-scheme heterojunction exhibited excellent TC antibiotic degradation efficiency, efficient and rapid OFLO antibiotic removal and *in-situ* H_2O_2 production rate. The absorption edge of the PDI-Urea/BiOBr composite photocatalyst red-shifted to around 800 nm, covering all the UV–vis region with part of the near infrared light region. The efficiency of 15% PDI-Urea/BiOBr for photodegraded TC or OFLO, photocatalytic production of H_2O_2 was significantly enhanced compared to either pure BiOBr or pure PDI-Urea. Moreover, the instantaneous generation of $^{\bullet}OH^-$, H_2O_2, h^+ and $^{\bullet}O_2^-$ during the photocatalytic process accelerates the decomposition of antibiotics through an efficient reductive oxidation process. The improved photocatalytic activity of PDI-Urea/BiOBr composite photocatalysts can be attributed to the construction of S-scheme heterojunctions with suitable band gap structure, extended light absorption range and excellent charge space separation efficiency. This work will provide a new idea for the design and construction of novel organic/inorganic heterojunction photocatalyst.

Declaration of competing interest

The authors declare that no conflict of interest exists in this paper.

Acknowledgments

The authors acknowledge the financial support from the National Natural Science Foundation of China (Nos. 51962023,

51862024), the Natural Science Foundation of Jiangxi Province, China (Nos. 20212BAB204045, 20192ACBL21047), the Key Laboratory of Jiangxi Province for Persistent Pollutants Control and Resources Recycle (Nanchang Hangkong University) (No. ES202002077).

Supplementary materials

Supplementary material associated with this article can be found, in the online version, at doi:10.1016/j.cclet.2022.01.058.

References

[1] J. Liu, X. Luo, Y. Sun, et al., Environ. Int. 126 (2019) 771–790.
[2] Y. Fu, Z. Ren, J. Wu, et al., Appl. Catal. B 285 (2021) 119785.
[3] Y. Zhou, J. Wang, X. Wei, et al., Sci. Total Environ. 782 (2021) 146603.
[4] M. Yin, Y. Zhou, D.C.W. Tsang, et al., J. Hazard. Mater. 407 (2021) 124402.
[5] A. Wang, Z. Zheng, H. Wang, et al., Appl. Catal. B 277 (2020) 119171.
[6] Q. Zhang, L. Jiang, J. Wang, et al., Appl. Catal. B 277 (2020) 119122.
[7] X. Xu, F. Deng, P. Shao, et al., Chem. Eng. J. 428 (2022) 132096.
[8] C. Wang, M. Cai, Y. Liu, et al., J. Colloid Interface Sci. 605 (2022) 727–740.
[9] Y. Xu, Y. Ma, X. Ji, et al., Appl. Surf. Sci. 464 (2019) 552–561.
[10] S. Dong, L. Cui, Y. Tian, et al., J. Hazard. Mater. 399 (2020) 123017.
[11] S. Dong, L. Xia, X. Chen, et al., Compos. Part B: Eng. 215 (2021) 108765.
[12] J. Chakraborty, I. Nath, C. Jabbour, et al., J. Hazard. Mater. 398 (2020) 122928.
[13] S. Li, C. Wang, M. Cai, et al., Chem. Eng. J. 428 (2022) 131158.
[14] S. Li, C. Wang, Y. Liu, et al., Chem. Eng. J. 415 (2021) 128991.
[15] Y. Yang, G. Zeng, D. Huang, et al., Appl. Catal. B 272 (2020) 118970.
[16] S. Li, C. Wang, Y. Liu, et al., Chem. Eng. J. 429 (2022) 132519.
[17] L.L. Albornoz, J.P. Bortolozzi, E.D. Banús, et al., Chem. Eng. J. 414 (2021) 128891.
[18] X. Liu, Z. Guo, L. Zhou, et al., Chemosphere 222 (2019) 38–45.
[19] S. Li, B. Xue, J. Chen, et al., Sep. Purif. Technol. 254 (2021) 117579.
[20] M. Zhu, L. Zhang, S. Liu, et al., Chin. Chem. Lett. 31 (2020) 1961–1965.
[21] S.F. Yin, C.T. Au, H. Li, Acta Phys. Chim. Sin. 36 (2020) 1910023.
[22] X. Li, J. Xiong, X. Gao, et al., J. Hazard. Mater. 387 (2020) 121690.
[23] P. Ding, H. Ji, P. Li, et al., Appl. Catal. B 300 (2022) 120633.
[24] K. Qin, Q. Zhao, H. Yu, et al., Environ. Res. 199 (2021) 111360.
[25] J. Xiong, X. Li, J. Huang, et al., Appl. Catal. B 266 (2020) 118602.
[26] Y. Li, Z. Lai, Z. Huang, et al., Appl. Surf. Sci. 550 (2021) 149342.
[27] X. Li, B. Wang, W. Yin, et al., Acta Phys. Chim. Sin. 36 (2020) 1902001.
[28] Y. Li, X. Li, H. Zhang, et al., J. Mater. Sci. Technol. 56 (2020) 69–88.
[29] M. Wang, J. Cheng, X. Wang, et al., Chin. J. Catal. 42 (2021) 37–45.
[30] X. Li, B. Kang, F. Dong, et al., Nano Energy 81 (2021) 105671.
[31] P. Wang, H. Li, Y. Cao, et al., Acta Phys. Chim. Sin. 37 (2021) 2008047.
[32] X. Ma, Q. Xiang, Y. Liao, et al., Appl. Surf. Sci. 457 (2018) 846–855.
[33] H. Yu, H. Ma, X. Wu, et al., Sol. RRL 5 (2021) 2000372.
[34] W. Zhong, X. Wu, Y. Liu, et al., Appl. Catal. B 280 (2021) 119455.
[35] X. Li, W. Wang, F. Dong, et al., ACS Catal. 11 (2021) 4739–4769.
[36] X. Yang, J. Yu, Y. Zhang, et al., J. Hazard. Mater. 381 (2020) 120994.
[37] Z. Jiang, Q. Chen, Q. Zheng, et al., Acta Phys. Chim. Sin. 37 (2021) 2010059.
[38] Z. Sun, X. Yang, X.F. Yu, et al., Appl. Catal. B 285 (2021) 119790.
[39] L. Guo, Y. Chen, Z. Ren, et al., Ultrason. Sonochem. 81 (2021) 105849.
[40] Y. Liu, Z. Zhang, Y. Fang, et al., Appl. Catal. B 252 (2019) 164–173.
[41] X. Li, J. Xiong, X. Gao, et al., J. Alloys Compd. 802 (2019) 196–209.
[42] J. Jia, C. Jiang, X. Zhang, et al., Appl. Surf. Sci. 495 (2019) 143524.
[43] P. Zhang, S. Zhang, D. Wan, et al., J. Hazard. Mater. 395 (2020) 122639.
[44] D. Liu, J. Wang, X. Bai, et al., Adv. Mater. 28 (2016) 7284–7290.
[45] X. Li, J. Liu, J. Huang, et al., Acta Phys. Chim. Sin. 37 (2021) 2010030.
[46] J. Yang, H. Miao, Y. Wei, et al., Appl. Catal. B 240 (2019) 225–233.
[47] Z. Zhang, Y. Zhu, X. Chen, et al., Adv. Mater. 31 (2019) 1806626.
[48] X. Li, J. Xiong, Y. Xu, et al., Chin. J. Catal. 40 (2019) 424–433.
[49] Z. Zhang, J. Wang, D. Liu, et al., ACS Appl. Mater. Inter. 8 (2016) 30225–30231.
[50] S. Zheng, S. Peng, Z. Wang, et al., Ceram. Int. 47 (2021) 28304–28311.
[51] P. Sharma, D. Damien, K. Nagarajan, et al., J. Phys. Chem. Lett. 4 (2013) 3192–3197.
[52] J. Wang, D. Liu, Y. Zhu, et al., Appl. Catal. B 231 (2018) 251–261.
[53] S. Dong, Y. Zhao, J. Yang, et al., Appl. Catal. B 291 (2021) 120127.
[54] Z. Zhang, X. Chen, H. Zhang, et al., Adv. Mater. 32 (2020) 1907746.
[55] G. Gupta, S.K. Kansal, Process Saf. Environ. Prot. 128 (2019) 342–352.
[56] J. Di, J. Xia, Y. Ge, et al., J. Mater. Chem. A 2 (2014) 15864–15874.
[57] Y. Wu, H. Ji, Q. Liu, et al., J. Hazard. Mater. 424 (2022) 127563.
[58] P. Li, Z. Zhou, Q. Wang, et al., J. Am. Chem. Soc. 142 (2020) 12430–12439.
[59] Z. Yao, H. Sun, Y. Hu, et al., J. Materiomics 7 (2021) 1122–1130.
[60] S. Juntrapirom, D. Tantraviwat, O. Thongsook, et al., Appl. Surf. Sci. 545 (2021) 149015.
[61] C. Zhang, M. Zhang, Y. Li, et al., Appl. Catal. B 248 (2019) 11–21.
[62] Y. Wang, Q. Liu, N.H. Wong, et al., Ceram. Int. 48 (2022) 2459-2469.
[63] Q. Xu, L. Zhang, B. Cheng, et al., Chem 6 (2020) 1543–1559.
[64] C. Liu, S. Mao, H. Wang, et al., Chem. Eng. J. 430 (2022) 132806.
[65] Q. Ji, Z. Xu, W. Xiang, et al., Chemosphere 253 (2020) 126751.
[66] X.A. Dong, W. Zhang, Y. Sun, et al., J. Catal. 357 (2018) 41–50.
[67] H. Dong, X. Guo, C. Yang, et al., Appl. Catal. B 230 (2018) 65–76.
[68] H. Li, T. Hu, N. Du, et al., Appl. Catal. B 187 (2016) 342–349.
[69] R. Wang, C. He, W. Chen, et al., Chin. Chem. Lett. 32 (2021) 3821-3824.
[70] R. Almeida, A. Banerjee, S. Chakraborty, et al., ChemPhysChem 19 (2018) 148–152.
[71] J. Wang, C. He, J. Huo, et al., Adv. Theor. Simul. 4 (2021) 2100003.
[72] J. Yu, C. He, C. Pu, et al., Chin. Chem. Lett. 32 (2021) 3149-3154.
[73] L. Wang, B. Cheng, L. Zhang, et al., Small 17 (2021) 2103447.
[74] Y. Wang, H. Huang, Z. Zhang, et al., Appl. Catal. B 282 (2021) 119570.
[75] B. Jin, X. Ye, H. Zhong, et al., Chin. Chem. Lett. 33 (2022) 812-816.
[76] X. Li, Y. Sun, T. Xiong, et al., J. Catal. 352 (2017) 102–112.
[77] Y. Yu, C. Cao, H. Liu, et al., J. Mater. Chem. A 2 (2014) 1677–1681.
[78] L. Wang, J. Zhang, Y. Zhang, et al., Small 18 (2022) 2104561.
[79] W. Liu, C. Song, M. Kou, et al., Chem. Eng. J. 425 (2021) 130615.